Romanian Reports in Physics **76**, 903 (2024)

THE BAND STRUCTURE OF HELICAL WAVEGUIDE ARRAYS IN TOPOLOGICAL PHOTONICS: A TUTORIAL

HUA ZHONG[1], DUMITRU MIHALACHE[2], SHUANG SHEN[1], YIQI ZHANG[1,*]

[1]Key Laboratory for Physical Electronics and Devices, Ministry of Education, School of Electronic Science and Engineering, Xi'an Jiaotong University, Xi'an 710049, China
[2]Horia Hulubei National Institute of Physics and Nuclear Engineering, 077125 Magurele, Bucharest, Romania
[*]Corresponding author, Email: *zhangyiqi@xjtu.edu.cn*

Received January 14, 2024

Abstract. The helical waveguide array is a well accepted model for fabricating the photonic topological insulator, since it introduces a gauge field to break the equivalent time-reversal symmetry of the system. However, there is a threshold, from both physical and mathematical point of view, for acquiring the corresponding band structure, especially for the beginners and even grown-up researchers. As far as we know, a tutorial on how to solve this problem is still absent from the scientific literature. To break the technique fence and provide a friendly documentation, we sort out this tutorial in detail based on our almost ten-year work experience in this area. Utilizing the tight-binding method with the nearest-neighbor coupling considered, we provide two methods to numerically calculate the band structure: the Floquet operator method and the Fourier expansion method. The main formulae and key codes are displayed. We believe this tutorial is a useful introduction in topological photonics and may be a shortcut for scientists who would like to venture into research areas related with topological physical objects.

Key words: topological photonics, helical waveguide array, band structure.

DOI: https://doi.org/10.59277/RomRepPhys.2024.76.903

1. INTRODUCTION

Topological photonics [1–9] is a new discipline that develops with the appearance of the photonic topological insulator, which is an optical analogue of the topological insulator in condensed matter physics [10, 11]. Since a topological insulator possesses unidirectional edge state that is topologically protected to be immune to disorders or defects, its photonic counterpart has been demonstrated to have a lot of potential applications in developing on-chip function devices [12]. The first photonic topological insulator was reported in a magneto-optical photonic crystal fabricated in the microwave regime [13]. However, a photonic topological insulator in visible optical wavelength regime that is independent on real magnetic field was not reported until 2013 [14]. In that milestone work, the crucial idea was the helical waveguide array that introduces a gauge field to break the equivalent time-reversal symmetry of

the system. Theoretical and experimental results have demonstrated the validity of the model and the uni-directional one-way topological edge state has been obtained that only couples among the surface waveguides [15].

The topological photonics is still in its everlasting development, and it attracts a lot of researchers from all over the world to participate in related topics. As one of the most classical model, the significance of the helical waveguide array model that mimics a periodically driven Floquet system [16, 17] is explicit. Until now, based on the modulated waveguide array model, topological edge solitons [18–26], topological edge lasing [27], topological protected photon path entanglement [28], anomalous topological phase [29, 30], to name just a few, have been delineated. However, it is not a easy task for a beginner to grasp the model in a short amount of time. One of the most frequently asked question is how to calculate for the band structure of the helical waveguide array? This question is crucial and fundamental since the band structure reflects the topological properties of the system. It is no exaggeration to say that one can never understand what is the topological insulator without inspecting the band structure firstly.

As the development of the topological photonics that inspires interdisciplinary research activities, a tutorial article on numerical methods to calculate the band structure becomes necessary. In this tutorial, we provide two methods to calculate for the band structure of the helical waveguide array. One is the Floquet operator method, and the other one is the Fourier expansion method. We not only give the formulae in detail, but also provide the key codes to execute related calculations. With this hand-holding tutorial, we believe the beginners and even experienced researchers would benefit greatly.

2. THEORETICAL MODEL

It is well accepted that the propagation of a light beam in a shallow lattice can be described by the Schrödinger-like paraxial wave equation

$$i\frac{\partial\psi}{\partial z} = -\frac{1}{2}\left(\frac{\partial^2}{\partial x^2} + \frac{\partial^2}{\partial y^2}\right)\psi - \mathcal{R}\left(x, y, z\right)\psi, \tag{1}$$

where x, y, x are the normalized coordinates, and $\mathcal{R}(x, y, z)$ represents the waveguide array, which can be depicted by Gaussian functions

$$\mathcal{R} = p\sum_{m,n}\exp\left(-\frac{\left[x - x_{m,n}(z)\right]^2 + \left[y - y_{m,n}(z)\right]^2}{d^2}\right), \tag{2}$$

where d is the waveguide width, $(x_{m,n}, y_{m,n})$ is the grid coordinate of the waveguide with the potential depth p that reflects the refractive index change. For a helical waveguide array [14], the grid coordinate is dependent on the propagation distance z,

as

$$\begin{cases} x_{m,n}(z) = x_{m,n}(0) + r_0 \sin(\Omega z) \\ y_{m,n}(z) = y_{m,n}(0) + r_0 \cos(\Omega z) - r_0, \end{cases} \tag{3}$$

where $\Omega = 2\pi/Z$ is the helical modulation frequency with Z being the helical period and r_0 is the helical radius. If we consider the rotating frame (x', y', z') with $x' = x - x_{m,n}(z)$, $y' = y - y_{m,n}(z)$ and $z' = z$, the z-dependent paraxial equation (1) can be rewritten as

$$i\left(\frac{\partial \psi}{\partial z'} - r_0\Omega\cos(\Omega z')\frac{\partial \psi}{\partial x'} + r_0\Omega\sin(\Omega z')\frac{\partial \psi}{\partial y'}\right) = \mathcal{R}(x', y')\psi - \frac{1}{2}\left(\frac{\partial^2}{\partial x'^2} + \frac{\partial^2}{\partial y'^2}\right)\psi. \tag{4}$$

If we introduce a vector potential $\boldsymbol{A}(z) = r_0\Omega\,[-\cos(\Omega z), \sin(\Omega z)]$, Eq. (4) can be rewritten as

$$i\frac{\partial \psi}{\partial z} = -\frac{1}{2}\left(\frac{\partial}{\partial x^2} + \frac{\partial}{\partial y^2} + i\boldsymbol{A}(z)\right)^2 \psi - \mathcal{R}\,(x, y)\,\psi - \frac{1}{2}r_0^2\Omega^2\psi. \tag{5}$$

For convenience, we still use (x, y, z) to represent the rotating frame from Eq. (5). Note that the last term in Eq. (5) just adds a uniform background to the lattice term. The vector potential $\boldsymbol{A}$ means that there is a gauge field, so the time-reversal symmetry of the system is broken, where the propagation distance z analogizes the evolution time in quantum mechanics. As a result, the helical waveguide array is adopted to mimic the Floquet mechanism [16, 17], and provides a promising platform for realizing the Chern topological insulator.

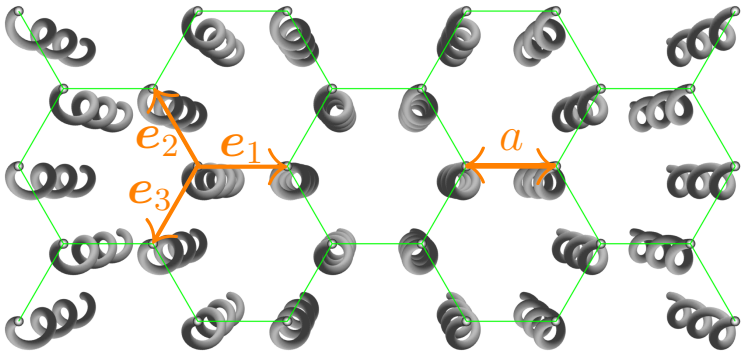

Fig. 1 – Schematic diagram of the helical waveguide array with a honeycomb lattice landscape.

If the lattice shape and the lattice depth are neglected, and the coupling only happens between two nearest-neighbor sites, one can utilize the tight-binding method to investigate the lattice property. In this tutorial, we take the honeycomb lattice, *i.e.* the photonic graphene, as the exemplary lattice that has two sublattices, and the schematic helical waveguide array is displayed in Fig. 1. The gray spring-like tubes

are the helical waveguides with a being the lattice constant and three typical vectors $\boldsymbol{e}_1 = [a, 0]$, $\boldsymbol{e}_2 = [-a/2, \sqrt{3}a/2]$, $\boldsymbol{e}_3 = [-a/2, -\sqrt{3}a/2]$. With the tight-binding method, the propagation dynamics of the light beam in the helical waveguide array is described by the discrete coupled equations

$$\begin{cases} i\dfrac{\partial \psi_{1,m,n}}{\partial z} &= \tau_1 \psi_{2,m+1,n} + \tau_2 \psi_{2,m-1,n+1} + \tau_3 \psi_{2,m-1,n-1}, \\ i\dfrac{\partial \psi_{2,m,n}}{\partial z} &= \tau_1^* \psi_{1,m-1,n} + \tau_2^* \psi_{1,m+1,n-1} + \tau_3^* \psi_{1,m+1,n+1}, \end{cases} \tag{6}$$

where $\tau_\nu = c\exp(i\boldsymbol{A}\cdot\boldsymbol{e}_\nu)$ with c being the coupling coefficient and ν representing 1, 2 or 3.

3. BAND STRUCTURE OF THE TWO-DIMENSIONAL (2D) HELICAL WAVEGUIDE ARRAY

Based on the coupled equations in (6), the Hamiltonian of the 2D helical honeycomb waveguide array can be written as

$$H(\boldsymbol{k}, z) = \begin{pmatrix} 0 & \mathcal{H}_{12} \\ \mathcal{H}_{21} & 0 \end{pmatrix}, \tag{7}$$

where $\mathcal{H}_{21} = \mathcal{H}_{12}^*$ and

$$\mathcal{H}_{12}(\boldsymbol{k}, z) = \sum_{\nu=1}^{3} \exp(i\boldsymbol{k}\cdot\boldsymbol{e}_\nu)\exp(i\boldsymbol{A}\cdot\boldsymbol{e}_\nu), \tag{8}$$

where $\boldsymbol{k} = [k_x, k_y]$ is the vector Bloch momentum. The second term in Eq. (8) is obtained based on the Peierls substitution [14]. With the Hamiltonian (7) at hand, we introduce two different methods to calculate the band structure of the helical waveguide array: the Floquet operator method and the Fourier expansion method.

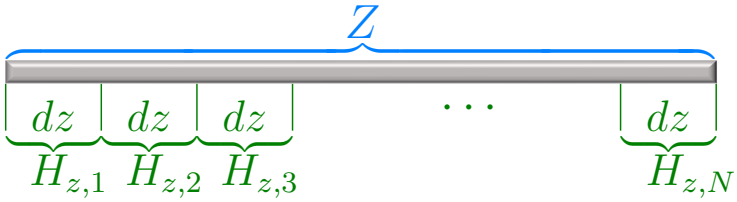

Fig. 2 – Schematic diagram of the Floquet operator method.

3.1. FLOQUET OPERATOR METHOD

The waveguide array is helical, so the Hamiltonian (7) is nowhere same in one longitudinal period. However, one can divide the waveguide into pieces, and each

piece is regarded as a straight waveguide array if each piece is sufficiently short. For example, as shown in Fig. 2, the waveguide is equally divided into N pieces with N being a big integer (*e.g.*, $N = 100$ or even larger), and the length of each piece is $dz = Z/N$. In this way, the Hamiltonians for each piece are:

$$\begin{cases} H_{z,1} = H(0), \\ H_{z,2} = H(dz), \\ H_{z,3} = H(2dz), \\ \cdots, \\ H_{z,N} = H[(N-1)dz]. \end{cases} \tag{9}$$

Therefore, the evolution operator can be written as

$$U(\boldsymbol{k}, Z) = \mathcal{Z} \prod_{\nu=1}^{N} \exp(-iH_{z,\nu}dz) = \exp[-iH_{\text{eff}}(\boldsymbol{k})Z], \tag{10}$$

where $\mathcal{Z}$ is the time-ordering operator and $H_{\text{eff}}(\boldsymbol{k})$ is the effective Hamiltonian of the Floquet system. Finally, one obtains the effective Hamiltonian

$$H_{\text{eff}}(\boldsymbol{k}) = \frac{i}{Z} \log[U(\boldsymbol{k}, Z)]. \tag{11}$$

The band structure of the helical waveguide array can be obtained by diagonalizing the effective Hamiltonian H_{eff}. The MATLAB code corresponding to Eqs. (10) and (11) is

```
H=zeros(2);
U=eye(2);
for z=0:dz:Z-dz
    A=r0*Omega*[-cos(Omega*z) sin(Omega*z)];
    kA=k+A;
    H(1,2)=exp(1i*kA*e1)+exp(1i*kA*e2)+exp(1i*kA*e3);
    H(2,1)=conj(H(1,2));
    U=expm(-1i*H*dz)*U;
end
Heff=1i/Z*logm(U);
```

According to the aforementioned explanations, the band structure of the helical honeycomb waveguide array can be numerically obtained. The band structures corresponding to $r_0 = 0$ and $r_0 = 0.15$ are shown in Figs. 3(a) and 3(b), respectively. One finds that there are six Dirac cones for the straight waveguide array with $r_0 = 0$, while if $r_0 = 0.15$, the Dirac cones disappear and a band gap emerges because of the gauge field introduced by the helix that represents the topological phase transition happens. The results are in accordance with those in Ref. [14].

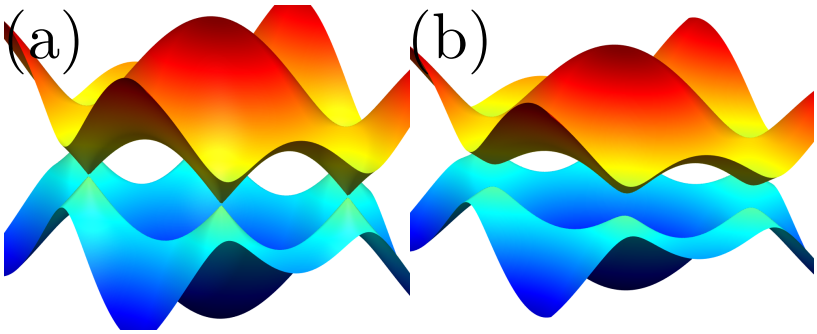

Fig. 3 – Band structure of the helical waveguide array with $\Omega = 6$ and $a = 1$ obtained based on the Floquet operator method: (a) $r_0 = 0$; (b) $r_0 = 0.15$.

3.2. FOURIER EXPANSION METHOD

According to the Hamiltonian (7), the dynamics of the light beam can be written in the form

$$i\frac{d}{dz}|\boldsymbol{\psi}\rangle = H(\boldsymbol{k}, z)|\boldsymbol{\psi}\rangle, \tag{12}$$

with $|\boldsymbol{\psi}\rangle$ being the amplitude vector of the beam [31, 32]. For the helical waveguide array with a longitudinal period Z, the solution of Eq. (12) can be written as $|\boldsymbol{\psi}\rangle = \exp(ibz)|\boldsymbol{\phi}\rangle$, with b being the quasi-propagation-constant and $|\boldsymbol{\phi}\rangle(z+Z) = |\boldsymbol{\phi}\rangle(z)$. Substituting $|\boldsymbol{\psi}\rangle$ by $|\boldsymbol{\phi}\rangle$, Eq. (12) can be rewritten as

$$i\frac{d}{dz}|\boldsymbol{\phi}\rangle - b|\boldsymbol{\phi}\rangle = H(\boldsymbol{k}, z)|\boldsymbol{\phi}\rangle. \tag{13}$$

Since the Hamiltonian (7) and $|\boldsymbol{\phi}\rangle$ are periodic functions of z with a period Z, they can be expanded as a Fourier series with different order harmonics, as follows

$$\begin{cases} \mathcal{H}_{12}(\boldsymbol{k}, z) = \sum\limits_{m=-f_m}^{f_m} H_{12,m}(\boldsymbol{k}) \exp(-im\Omega z), \\ \mathcal{H}_{21}(\boldsymbol{k}, z) = \sum\limits_{m=-f_m}^{f_m} H_{21,m}(\boldsymbol{k}) \exp(-im\Omega z), \\ |\boldsymbol{\phi}\rangle = \sum\limits_{m=-f_m}^{f_m} |\boldsymbol{\phi}_m\rangle \exp(-im\Omega z), \end{cases} \tag{14}$$

where the Fourier coefficients are

$$\begin{cases} H_{12,m}(\boldsymbol{k}) = \dfrac{1}{Z}\displaystyle\int_0^Z \mathcal{H}_{12}(\boldsymbol{k},z)\exp(im\Omega z)dz, \\ H_{21,m}(\boldsymbol{k}) = \dfrac{1}{Z}\displaystyle\int_0^Z \mathcal{H}_{21}(\boldsymbol{k},z)\exp(im\Omega z)dz, \\ |\boldsymbol{\phi}_m\rangle = \dfrac{1}{Z}\displaystyle\int_0^Z |\boldsymbol{\phi}\rangle\exp(im\Omega z)dz. \end{cases} \tag{15}$$

Here m is an integer that takes the value in $[-f_m, +f_m]$ with f_m being a sufficiently large positive integer. The Matlab code for Eq. (15) is:

```
for m=-fm:fm
    H12(m+fm+1)=1/Z*sum(exp(1i*m*Omega*z).*H(1,2))*dz;
    H21(m+fm+1)=1/Z*sum(exp(1i*m*Omega*z).*H(2,1))*dz;
end
```

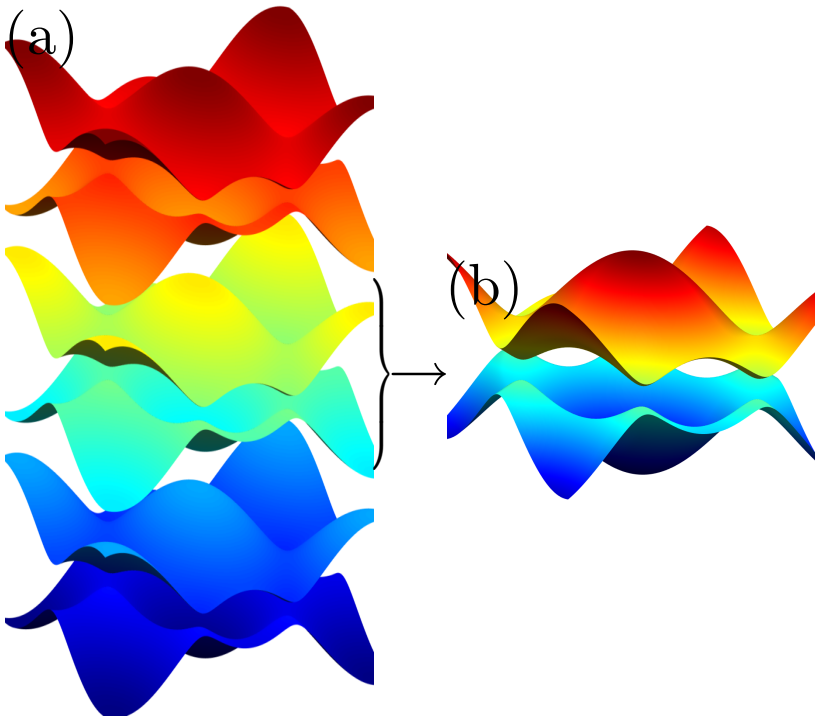

Fig. 4 – Band structure of the helical waveguide array with $\Omega = 6$, $a = 1$, and $r_0 = 0.15$ by using the Fourier expansion method in three longitudinal Brillouin zones (a) and in one longitudinal Brillouin zone (b).

Inserting Eq. (14) into Eq. (13) and considering $|\boldsymbol{\phi}_m\rangle = [|\phi_m^A\rangle, |\phi_m^B\rangle]$, one

obtains

$$\begin{cases} m\Omega|\phi_m^A\rangle - \sum_k |\phi_{m-k}^B\rangle H_{12,k} = b|\phi_m^A\rangle, \\ m\Omega|\phi_m^B\rangle - \sum_k |\phi_{m-k}^A\rangle H_{21,k} = b|\phi_m^B\rangle. \end{cases} \tag{16}$$

We write out all the coupled equations in (16) from $m = -f_m$ to $m = +f_m$, and we rewrite them into matrix format. Then one obtains

$$\begin{bmatrix} M_0 & M_{12} \\ M_{21} & M_0 \end{bmatrix} |\boldsymbol{\phi}_{1\sim N}\rangle = H_M |\boldsymbol{\phi}_{1\sim N}\rangle = b|\boldsymbol{\phi}_{1\sim N}\rangle, \tag{17}$$

with $|\boldsymbol{\phi}_{1\sim N}\rangle = [|\phi_{-f_m}^A\rangle, \cdots, |\phi_{f_m}^A\rangle, |\phi_{-f_m}^B\rangle, \cdots, |\phi_{f_m}^B\rangle]^{\mathrm{T}}$. Diagonalizing the matrix H_M in Eq. (17), one obtains the quasi-propagation-constant b, that is, the band structure of the helical waveguide array, as shown in Fig. 4(a) that gives the band structure in three (there are $2f_m + 1$ in total) longitudinal Brillouin zones. If the value of b is confined in the window $-\Omega/2 \leq b \leq \Omega/2$, the band structure is shown in Fig. 4(b), that is, the same as that shown in Fig. 3(b). The corresponding MATLAB code is:

```
M0=diag([-fm:fm]*Omega);
M12=diag(ones(1,2*fm+1)*H12(fm+1));
M21=diag(ones(1,2*fm+1)*H21(fm+1));
for fl=1:fm
    M12=M12+diag(ones(1,2*fm+1-fl)*H12(fm+1-fl),fl) + ...
        diag(ones(1,2*fm+1-fl)*H12(fm+1+fl),-fl);
    M21=M21+diag(ones(1,2*fm+1-fl)*H21(fm+1-fl),fl) + ...
        diag(ones(1,2*fm+1-fl)*H21(fm+1+fl),-fl);
end
HM=[M0 M12;M21 M0];
```

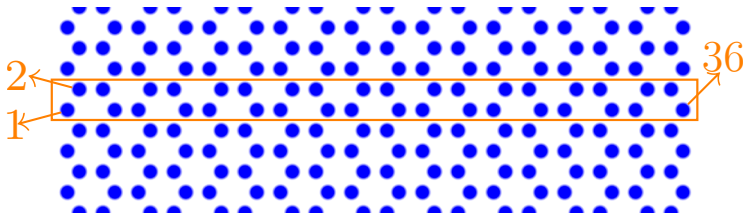

Fig. 5 – Schematic diagram of the honeycomb lattice with zigzag boundaries. The lattice is periodic in y. The orange rectangle indicates the calculation unit cell, in which the sites are numbered from left to right.

4. BAND STRUCTURE OF THE 1D HELICAL WAVEGUIDE ARRAY

Different from the 2D case, the one-dimensional (1D) lattice is truncated in the x or y direction, which only left one Bloch momentum be a good quantum number. For example, the honeycomb lattice in Fig. 5 is truncated in x direction with a zigzag boundary and periodic in y, so only k_y is a good quantum number and $\boldsymbol{k} = [0, k_y]$. For the 2D case, there are two sites in one unit cell that has a rhombic shape. While for the 1D case, the unit cell is quite different. In Fig. 5, the unit cell is indicated by an orange rectangle that has 36 sites, which are numbered from left to right.

If we assume 4 sites a group, then there are nine groups for the unit cell in Fig. 5. The transient Hamiltonian of the system with one group can be written as

$$H(\boldsymbol{k}, z) = \begin{bmatrix} 0 & H_{12} & 0 & 0 \\ H_{12}^* & 0 & H_{23} & 0 \\ 0 & H_{23}^* & 0 & H_{12} \\ 0 & 0 & H_{12}^* & 0 \end{bmatrix}, \tag{18}$$

where $H_{12} = \exp(-i\boldsymbol{k}\cdot\boldsymbol{e}_2)\exp(-i\boldsymbol{A}\cdot\boldsymbol{e}_2) + \exp(-i\boldsymbol{k}\cdot\boldsymbol{e}_3)\exp(-i\boldsymbol{A}\cdot\boldsymbol{e}_3)$ and $H_{23} = \exp(i\boldsymbol{k}\cdot\boldsymbol{e}_1)\exp(i\boldsymbol{A}\cdot\boldsymbol{e}_1)$. In this way, the Hamiltonian for N groups can be easily obtained.

If the Floquet operator method is adopted, the corresponding Matlab code is:

```
k=[0 ky];
H=zeros(4*N);
U=eye(4*N);
for z=0:dz:zL-dz
    A=r0*Omega*[-cos(Omega*z) sin(Omega*z)];
    kA=k+A;
    M=(exp(-1i*kA*e3)+exp(-1i*kA*e2))*ones(1,4*N-1);
    M(2:2:4*N-2)=exp(1i*kA*e1);
    H=diag(M,1)+diag(conj(M),-1);
    U=expm(-1i*H*dz)*U;
end
Heff=1i/Z*logm(U);
```

If the Fourier expansion method is adopted, the MATLAB code is:

```
A=r0*Omega*[-cos(Omega*z) sin(Omega*z)];
kA=k+A;
H1=exp(-1i*kA*e1);
H2=exp(-1i*kA*e2);
H3=exp(-1i*kA*e3);
for m=-fm:fm
    H12(m+fm+1)=1/Z*sum(exp(1i*Omega*m*z).*(H2+H3))*dz;
```

```
    H21(m+fm+1)=1/Z*sum(exp(1i*Omega*m*z).*conj(H2+H3))*dz;
    H23(m+fm+1)=1/Z*sum(exp(1i*Omega*m*z).*conj(H1))*dz;
    H34(m+fm+1)=1/Z*sum(exp(1i*Omega*m*z).*(H2+H3))*dz;
    H32(m+fm+1)=1/Z*sum(exp(1i*Omega*m*z).*H1)*dz;
    H43(m+fm+1)=1/Z*sum(exp(1i*Omega*m*z).*conj(H2+H3))*dz;
end
M0=diag([-fm:fm]*Omega);
M12=diag(ones(1,2*fm+1)*H12(fm+1));
M21=diag(ones(1,2*fm+1)*H21(fm+1));
M23=diag(ones(1,2*fm+1)*H23(fm+1));
M32=diag(ones(1,2*fm+1)*H32(fm+1));
M34=diag(ones(1,2*fm+1)*H34(fm+1));
M43=diag(ones(1,2*fm+1)*H43(fm+1));
for fl=1:fm
    M12=M12+diag(ones(1,2*fm+1-fl)*H12(fm+1-fl),fl)+...
        diag(ones(1,2*fm+1-fl)*H12(fm+1+fl),-fl);
    M21=M21+diag(ones(1,2*fm+1-fl)*H21(fm+1-fl),fl)+...
        diag(ones(1,2*fm+1-fl)*H21(fm+1+fl),-fl);
    M23=M23+diag(ones(1,2*fm+1-fl)*H23(fm+1-fl),fl)+...
        diag(ones(1,2*fm+1-fl)*H23(fm+1+fl),-fl);
    M32=M32+diag(ones(1,2*fm+1-fl)*H32(fm+1-fl),fl)+...
        diag(ones(1,2*fm+1-fl)*H32(fm+1+fl),-fl);
    M34=M34+diag(ones(1,2*fm+1-fl)*H34(fm+1-fl),fl)+...
        diag(ones(1,2*fm+1-fl)*H34(fm+1+fl),-fl);
    M43=M43+diag(ones(1,2*fm+1-fl)*H43(fm+1-fl),fl)+...
        diag(ones(1,2*fm+1-fl)*H43(fm+1+fl),-fl);
end
HM1=[M0 M12;M21 M0];
HM2=[M0 M34;M43 M0];
for flag=1:2:N
    index1=2*(2*fm+1)*flag-(2*(2*fm+1)-1):2*(2*fm+1)*flag;
    Hfinal(index1,index1)=HM1;
end
for flag=1:2:N-1
    index2=2*(2*fm+1)*flag+1:2*(2*fm+1)*(flag+1);
    Hfinal(index2,index2)=HM2;
end
for flag=1:N-1
    index3=2*(2*fm+1)*flag-2*fm:2*(2*fm+1)*flag;
    index4=2*(2*fm+1)*flag+1:2*(2*fm+1)*flag+(2*fm+1);
```

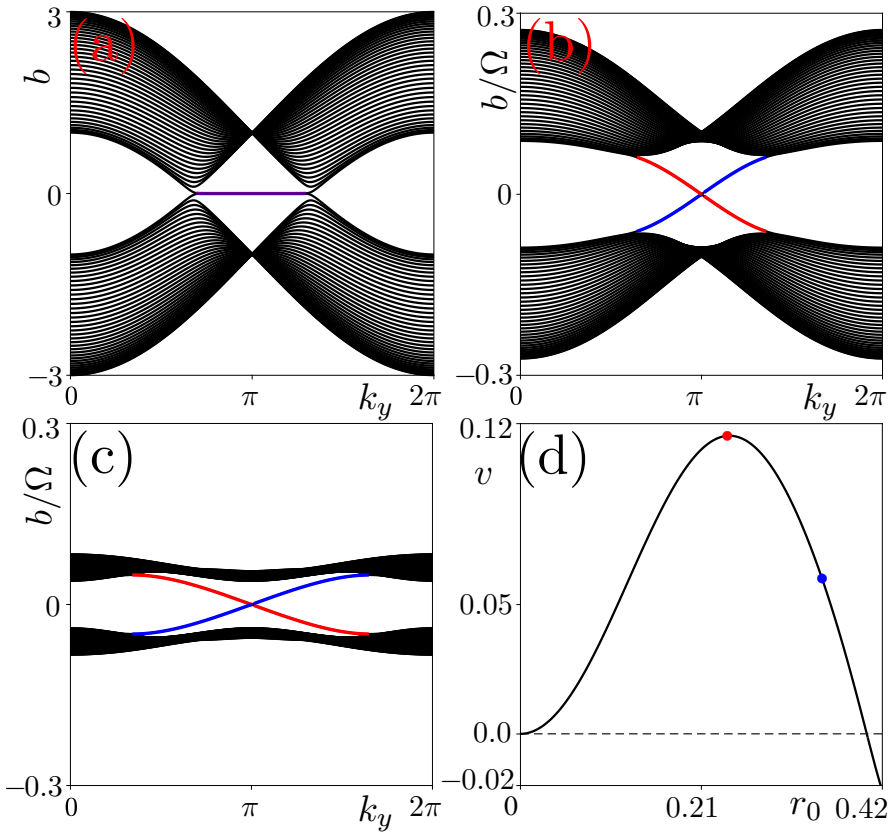

Fig. 6 – Band structure of the honeycomb lattice with zigzag boundaries in x and periodic in y. Black curves are for the bulk states while the red and blue curves are for the edge states: (a) $r_0 = 0$; (b) $r_0 = 0.24$; (c) $r_0 = 0.35$; (d) the group velocity *versus* r_0 of the red topological edge state at $k_y = \pi$.

```
    Hfinal(index3,index4)=M23;
    Hfinal(index4,index3)=M32;
end
```

The related band structures with 1D zigzag boundaries under different helix r_0 are shown in Fig. 6. If the radius is 0, the helical waveguide array reduces to a straight waveguide array, and the band structure is indicated by Fig. 6(a) — there are two degenerated edge states as highlighted by red and blue colors. While if the radius becomes nonzero, the edge states are not degenerated any longer, as shown by the edge states in Figs. 6(b) and 6(c), which correspond to $r_0 = 0.24$ and $r_0 = 0.35$, respectively. However, the moving speed of the edge states $v = -db/dk_y$ changes with r_0 since the slope of the edge states does not hold. In Fig. 6(d), we display the moving speed v as a function of r_0 of red topological edge states at $k_y = \pi$.

One finds that the speed v firstly increases with r_0 and reaches a maximum value at $k_y \sim 0.24$ as indicated by the red dot corresponding to Fig. 6(b). Further increasing the radius r_0, the moving speed of the edge state decreases monotonously [the blue dot is corresponding to Fig. 6(c)]. If the radius reaches $r_0 \sim 0.40$, the moving speed is ~ 0, which means that the band gap closes again. The result in Fig. 6(d) is in accordance with that in Ref. [14].

5. CONCLUSION

Summarizing, we have introduced the numerical methods to calculate the band structure of the helical waveguide array in detail. Both the Floquet operator method and the Fourier expansion method are discussed with the key MATLAB code presented. The numerical methods are feasible and correct since the band structures are the same as those reported in the previous scientific literature. This tutorial article provides a shortcut for beginners. We believe it is also a valuable and a beneficial reference for researchers in other areas who plan to venture into the topological photonics and other physical subfields connected with the topological insulators. At last, we would like to note that the band structures of various lattice waveguide arrays, such as the kagome lattice [33, 34], the Lieb lattice [35, 36], the superhoneycomb lattice [37], and the lattice with type-II Dirac cones [38], can be obtained by using the numerical methods described in this tutorial article.

Acknowledgements. This work is supported by the National Natural Science Foundation of China (12304370, 12074308) and the Fundamental Research Funds for the Central Universities (xzy022023059).

REFERENCES

1. L. Lu, J. D. Joannopoulos and M. Soljačić, Nat. Photon. **8**(11), 821–829 (2014).
2. T. Ozawa *et al.*, Rev. Mod. Phys. **91**, 015006 (2019).
3. D. Smirnova, D. Leykam, Y. Chong, and Y. Kivshar, Appl. Phys. Rev. **7**(2), 021306 (2020).
4. M. Segev and M. A. Bandres, Nanophoton. **10**(1), 425–434 (2021).
5. M. Parto, Y. G. N. Liu, B. Bahari, M. Khajavikhan, and D. N. Christodoulides, Nanophoton. **10**(1), 403–423 (2021).
6. H. Wang, X. Zhang, J. Hua, D. Lei, M. Lu, and Y. Chen, J. Opt. **23**(12), 123001 (2021).
7. Q. Yan, X. Hu, Y. Fu, C. Lu, C. Fan, Q. Liu, X. Feng, Q. Sun, and Q. Gong, Adv. Opt. Mater. **9**, 2001739 (2021).
8. Z.-K. Lin, Q. Wang, Y. Liu, H. Xue, B. Zhang, Y. Chong, and J.-H. Jiang, Nat. Rev. Phys. **5**(8), 483–495 (2023).
9. X. Zhang, F. Zangeneh-Nejad, Z.-G. Chen, M.-H. Lu, and J. Christensen, Nature **618**(7966), 687–697 (2023).
10. M. Z. Hasan and C. L. Kane, Rev. Mod. Phys. **82**, 3045–3067 (2010).

11. X.-L. Qi and S.-C. Zhang, Rev. Mod. Phys. **83**, 1057–1110 (2011).
12. C.-C. Lu, H.-Y. Yuan, H.-Y. Zhang, W. Zhao, N.-E. Zhang, Y.-J. Zheng, S. Elshahat, and Y.-C. Liu, Chip **1**(4), 100025 (2022).
13. Z. Wang, Y. Chong, J. D. Joannopoulos, and M. Soljačić, Nature **461**, 772–775 (2009).
14. M. C. Rechtsman, J. M. Zeuner, Y. Plotnik, Y. Lumer, D. Podolsky, F. Dreisow, S. Nolte, M. Segev, and A. Szameit, Nature **496**, 196–200 (2013).
15. Y. Chong, Nature **496**(7444), 173–174 (2013).
16. M. S. Rudner, N. H. Lindner, E. Berg, and M. Levin, Phys. Rev. X **3**, 031005 (2013).
17. M. S. Rudner and N. H. Lindner, Nat. Rev. Phys. **2**(5), 229–244 (2020).
18. Y. Lumer, Y. Plotnik, M. C. Rechtsman, and M. Segev, Phys. Rev. Lett. **111**, 243905 (2013).
19. D. Leykam and Y. D. Chong, Phys. Rev. Lett. **117**, 143901 (2016).
20. M. J. Ablowitz and J. T. Cole, Phys. Rev. A **96**, 043868 (2017).
21. M. J. Ablowitz and J. T. Cole, Phys. Rev. A **99**, 033821 (2019).
22. S. Mukherjee and M. C. Rechtsman, Science **368**(6493), 856–859 (2020).
23. S. K. Ivanov, Y. V. Kartashov, A. Szameit, L. Torner, and V. V. Konotop, ACS Photon. **7**(3), 735–745 (2020).
24. S. K. Ivanov, Y. V. Kartashov, L. J. Maczewsky, A. Szameit, and V. V. Konotop, Opt. Lett. **45**(6), 1459–1462 (2020).
25. S. K. Ivanov, Y. V. Kartashov, L. J. Maczewsky, A. Szameit, and V. V. Konotop, Opt. Lett. **45**(8), 2271–2274 (2020).
26. S. K. Ivanov, Y. V. Kartashov, M. Heinrich, A. Szameit, L. Torner, and V. V. Konotop, Phys. Rev. A **103**, 053507 (2021).
27. S. K. Ivanov, Y. Q. Zhang, Y. V. Kartashov, and D. V. Skryabin, APL Photon. **4**(12), 126101 (2019).
28. M. C. Rechtsman, Y. Lumer, Y. Plotnik, A. Perez-Leija, A. Szameit, and M. Segev, Optica **3**(9), 925–930 (2016).
29. S. Mukherjee, A. Spracklen, M. Valiente, E. Andersson, P. Öhberg, N. Goldman, and R. R. Thomson, Nat. Commun. **8**, 13918 (2017).
30. L. J. Maczewsky, J. M. Zeuner, S. Nolte, and A. Szameit, Nat. Commun. **8**, 13756 (2017).
31. K. Fang, Z. Yu, and S. Fan, Opt. Express **21**, 18216–18224 (2013).
32. K. Fang, Z. Yu, and S. Fan, Nat. Photon. **6**(11), 782–787 (2012).
33. H. Zhong, R. Wang, F. Ye, J. W. Zhang, L. Zhang, Y. P. Zhang, M. R. Belić, and Y. Q. Zhang, Results Phys. **12**, 996–1001 (2019).
34. Q. Tang, B. Q. Ren, M. R. Belić, Y. Q. Zhang, and Y. D. Li, Rom. Rep. Phys. **74**, 405 (2022).
35. M. A. Bandres, M. Rechtsman, A. Szameit, and M. Segev, in *CLEO: 2014*, p. FF2D.3 (Optical Society of America, 2014).
36. Y. Q. Zhang, X. Liu, M. Belić, W. P. Zhong, C. B. Li, H. X. Chen, and Y. P. Zhang, Rom. Rep. Phys. **68**, 230–240 (2016).
37. H. Zhong, Y. Q. Zhang, Y. Zhu, D. Zhang, C. B. Li, Y. P. Zhang, F. L. Li, M. R. Belić, and M. Xiao, Ann. Phys. (Berlin) **529**(3), 1600258 (2017).
38. H. Zhong, S. Xia, Y. Li, Y. Zhang, D. Song, C. Liu, and Z. Chen, Adv. Photon. **3**(5), 056001 (2021).